Response of Composite Material Shallow Arch to Concentrated Load

Eric R. Johnson*
Virginia Polytechnic Institute and State University, Blacksburg, Virginia
Michael W. Hyer†
University of Maryland, College Park, Maryland
and
Douglas M. Carper‡
Pratt and Whitney Aircraft, Middletown, Connecticut

The large displacement static response of shallow, specially orthotropic composite panels subjected to lateral loading is examined both theoretically and experimentally. The panels are thin, circular cylindrical shells with the straight edges simply supported at a fixed distance apart, and the curved edges are free. The lateral load is a spatially uniform line load acting along the generator, or axial, direction of the cylinder, and it is directed radially inward toward the center. Under the conditions described, the response of the panel is independent of the axial coordinate, and is dependent on the circumferential coordinate only. Hence, the panel analysis is one-dimensional, and it is qualitatively the same as a shallow circular arch under a concentrated load. The load induces a circumferential thrust, and the panel can, and does, snap-through to an inverted configuration at the buckling load. The influence of load position on the response is also examined. A test fixture was carefully designed to duplicate these conditions. The test panels discussed are $[(90/0)_3]_s$ graphite-epoxy laminates. Very good agreement between theory and experiment is achieved. Much of the discrepancy between theory and experiment is due to geometric imperfections in the initial shape of the panels tested.

Nomenclature

A,B,C,D = dimensionless coefficients in the quadratic Eqs. (37), (39), and (41), which are functions of the thrust parameter q
A_n^* = dimensionless amplitude in Eq. (33) determined from Eq. (37)
A_{22} = laminate extensional stiffness in the circumferential direction
b = dimensionless asymmetric amplitude in Eq. (34) determined by Eq. (39)
D_{22} = laminate bending stiffness in the circumferential direction
H = midspan arch rise; see Fig. 1
h = panel thickness
L_x = axial length of panel
L_s = distance between immovable supports; see Fig. 1
M_θ = circumferential bending moment per unit axial length
N_θ = circumferential force resultant per unit axial length
n = positive integer
O = center of circular cross section; see Fig. 1
P = radial line load force intensity per unit axial length
p = dimensionless load intensity defined by Eq. (12)
q = dimensionless thrust parameter defined in Eq. (28)
q_n = $n\pi/2$; specific values of q
R = radius of circular middle surface; see Fig. 1
U = strain energy
u,w = circumferential and inward radial displacement components, respectively, for a point on the middle surface
$\bar{u}$ = dimensionless circumferential displacement
x = axial shell coordinate; $0 \le x \le L_x$
z = radial, or normal, shell middle surface coordinate; $|z| \le h/2$
β = semiopening angle; see Fig. 1
β_θ = out-of-plane rotation of a circumferential line element in the middle surface
Γ = normalized polar angle, $|\Gamma| \le 1$, see Eq. (8)
$\bar{\Gamma}$ = value of Γ at the position of the radial line load, $|\bar{\Gamma}| < 1$
ϵ_θ = normal strain of a circumferential line element in the middle surface
η = dimensionless circumferential force resultant, see Eq. (11)
θ = polar angle, $|\theta| \le \beta$; see Fig. 1
$\bar{\theta}$ = circumferential location of radial line load
κ = change in curvature of a circumferential line element in the middle surface
λ = dimensionless arch rise parameter, see Eq. (15)
ξ = dimensionless load parameter defined by Eq. (29)
Π = potential energy
$\bar{\Pi}$ = dimensionless potential energy, see Eq. (13)
π = ratio of the length of the circumference of a circle to its diameter
ϕ = dimensionless radial displacement defined in Eq. (9)

Superscripts

$(\,)'$ = derivative of $(\,)$ with respect to Γ
$(\,)^+$ = evaluation of $(\,)$ as $\Gamma \to \bar{\Gamma}$ for $\Gamma > \bar{\Gamma}$
$(\,)^-$ = evaluation of $(\,)$ as $\Gamma \to \bar{\Gamma}$ for $\Gamma > \bar{\Gamma}$

Presented as Paper 84-0594 at the AIAA/ASME/ASCE/AHS 25th Structures, Structural Dynamics and Materials Conference, Palm Springs, CA, May 14-16, 1984; received July 15, 1984, revision received Feb. 11, 1985.

*Assistant Professor of Aerospace and Ocean Engineering. Member AIAA.
†Professor of Mechanical Engineering. Member AIAA.
‡Materials Engineer, Materials Engineering and Research Department. Member AIAA.

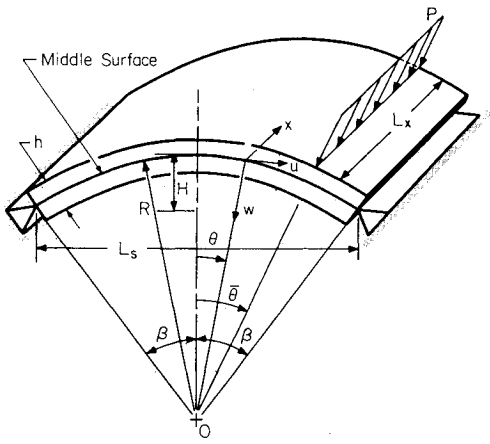

Fig. 1 Cylinder geometry and nomenclature.

Introduction

THE results of an analytical and experimental study on the large displacement response of circular cylindrical panels fabricated from graphite-epoxy unidirectional tape are presented. The study was motivated by the concern for the crashworthiness of composite fuselage structures in which large displacements occur due to lateral impact loads. Insufficient data on the large deflection response of advance composite structures subject to lateral loads suggested that the study focus on the large displacement static behavior of a single component. For this reason circular cylindrical panels were selected whose radii, thickness, and circumferential arc lengths are representative of fuselage panels mounted between frames and stringers of transport aircraft. Consequently, the panels are thin and shallow.

The lateral loading is represented by a spatially uniform line load acting along the generator of the cylinder. It is directed radially inward toward the center of curvature (see Fig. 1). The straight edges of the panels are simply supported at a fixed distance apart, and the curved edges are free. In this situation the lateral load induces a circumferential thrust in the panel, and snap-through instability can, and does, occur. During snap-through the panel displaces to a fully inverted configuration. Thus, the displacements are on the order of twice the maximum midspan rise of the panel (dimension H in Fig. 1).

A test fixture was carefully designed to duplicate the conditions described. However, the loading device is designed to provide control of the displacement at the line of application rather than control the magnitude of the force. This is an advantage because a greater portion of the load-displacement equilibrium path is stable for displacement-controlled loading than for force-controlled loading. Thus, limit point loads (relative maximum loads) on the equilibrium path can be precisely determined with this experimental setup.

The nominal radius of all panels tested is 60 in., the thickness ranging from 0.022 to 0.084 in., and the arc lengths are either 6 or 12 in. The panels are 3 in. wide. Only the results from the panels with a nominal thickness of 0.060 in. and 12-in. arc lengths are reported here. Since the trends observed for the panels tested were similar, the test cases presented herein are representative. See Ref. 1 for the remaining test results.

The response of the panel is independent of the generator, or axial, direction. Consequently, the mathematical analysis is one-dimensional in the circumferential coordinate. In fact, the mathematical analysis for the panels in this study is identical to the analysis of a shallow circular arch. Physically the panel response is stiffer than the arch response, since the axial strain is assumed to vanish for the panel, whereas the transverse normal stress is assumed to vanish for the arch. Thus, it is appropriate to review the literature on shallow arches.

Static Response of Shallow Arches

References 2-7 document the essential features of the response of shallow arches made from homogeneous, isotropic, and linear elastic materials. For symmetry of the initial shape, lateral load, and end conditions about midspan, the arch will snap-through at either a limit point or a bifurcation point on the equilibrium path. Biezeno and Grammel[2] have presented results for the symmetric response of a shallow circular arch with pinned ends subject to a concentrated load at midspan. Fung and Kaplan[3] have conducted a complete investigation into shallow arches using a Fourier series solution, and have presented exact results for a sinusoidal arch with sinusoidal loading and pinned ends. Schreyer and Masur[4] analyzed the equilibrium, and stability of equilibrium, for clamped shallow circular arches under uniform pressure and a concentrated load. Whether instability occurs at a limit or bifurcation point depends upon the midspan rise of the arch. For very shallow arches all equilibrium configurations are stable. A deeper arch loses stability at a limit point, and, as the rise further increases, the instability occurs at a bifurcation point. The bifurcation point is the intersection of the primary equilibrium path with a secondary path. The secondary path represents asymmetric equilibrium configurations.

Cheung and Babcock[5] have presented experimental data on the effects of load eccentricity, or offset, with respect to midspan location for shallow circular arches with clamped ends subjected to a concentrated load. They found that the snap-through buckling load was reduced for small load eccentricities. Schreyer[6] has presented an analysis of initial shape imperfections and load eccentricities for the clamped circular arch in the experimental study of Cheung and Babcock. Both imperfections in initial shape and small load eccentricities reduced the snap-through buckling load with respect to the perfect case (no imperfections or eccentricity). Plaut[7] studied the question of the position of a concentrated load on the stability of a shallow circular arch with various end conditions. Arches that lose stability at bifurcation points when the load is exactly at midspan are very sensitive to small load eccentricities. That is, small eccentricities in the load from the midspan position cause a rapid decrease in the buckling load.

Significantly less work has been done on the snap-through stability of shallow orthotropic and/or anisotropic structures. Nash and Hsu[8] analyzed the static response of a shallow circular arch fabricated from a filamentary composite material with the fiber direction normal to the middle surface. They included transverse shear and transverse normal stress effects. In this case, the qualitative behavior was found similar to the isotropic arch in the respect that the response was determined by a geometric parameter (arch rise). Marshall et al.[9] have studied the static response of spherically curved glass-epoxy panels both experimentally and analytically. Good correlation between theory and experiment was reported.

Analysis

Governing Equations

The derivation of the equations for shallow arches can be found in Refs. 3, 4, and 10. The derivation here does not lead to new equilibrium equations, but is presented for reasons of completeness and to introduce laminated composite material properties into the analysis. For a specially orthotropic, circular cylindrical panel deforming into another cylindrical configuration, only the circumferential strain is nonzero. The nonlinear strain-displacement equations for small strains and moderate rotations of the middle surface of a shallow cylindrical panel are

$$\epsilon_\theta = \frac{1}{R}\left(\frac{du}{d\theta} - w\right) + \tfrac{1}{2}\beta_\theta^2 \tag{1}$$

$$\beta_\theta = \frac{1}{R}\frac{dw}{d\theta} \tag{2}$$

$$\kappa = \frac{1}{R}\frac{d\beta_\theta}{d\theta} \tag{3}$$

The panel is a symmetric bidirectional laminate with the material axes parallel to the x and θ directions. From classical lamination theory the constitutive equations for this case reduce to

$$N_\theta = A_{22}\epsilon_\theta \tag{4}$$

$$M_\theta = D_{22}\kappa \tag{5}$$

In cylindrical deformation, the strain energy for the panel is

$$U = \left(\frac{L_x}{2}\right)\int_{-\beta}^{+\beta} (N_\theta\epsilon_\theta + M_\theta\kappa)R\,d\theta \tag{6}$$

The total potential energy is

$$\Pi = U - L_x P w(\bar{\theta}) \tag{7}$$

After Eqs. (1-6) are substituted into Eq. (7), the potential energy is a functional of displacements u and w. This expression is written in dimensionless form by defining

$$\Gamma = \theta/\beta \tag{8}$$

$$\phi = w/(R\beta^2) \tag{9}$$

$$\bar{u} = u/(R\beta^3) \tag{10}$$

$$\eta = N_\theta/(A_{22}\beta^2) \tag{11}$$

$$p = P/(A_{22}\beta^3) \tag{12}$$

$$\tilde{\Pi} = \pi/(L_x R A_{22}\beta^5) \tag{13}$$

Thus, the dimensionless potential is

$$\tilde{\Pi} = \tfrac{1}{2}\int_{-1}^{+1} [\eta^2 + \lambda^{-4}(\phi'')^2]\,d\Gamma - p\phi(\bar{\Gamma}) \tag{14}$$

in which derivatives with respect to Γ are denoted by primes, and the dimensionless parameter λ is defined by

$$\lambda^4 = A_{22}R^2\beta^4/D_{22} \tag{15}$$

Also from Eqs. (1) and (2) and (8-11), the dimensionless strain-displacement equation becomes

$$\eta = \bar{u}' - \phi + (1/2)(\phi')^2 \tag{16}$$

Stationarity of the potential energy functional leads to the equilibrium differential equations

$$\eta' = 0 \tag{17}$$

$$\lambda^{-4}\phi'''' - \eta(1+\phi'') = 0 \tag{18}$$

Equation (17) shows the dimensionless force resultant is spatially constant. A convenient expression for η in terms of ϕ is obtained by integrating Eq. (16) from -1 to $+1$, and recognizing that the circumferential displacements vanish at $\Gamma = \pm 1$. Thus,

$$\eta = -\tfrac{1}{2}\int_{-1}^{+1} [\phi - \tfrac{1}{2}(\phi')^2]\,d\Gamma \tag{19}$$

Equations (18) and (19) are to be solved subject to the pin-ended boundary conditions and the transition conditions at the position of the applied load. The boundary conditions are

$$\phi(\pm 1) = 0 \tag{20}$$

$$\phi''(\pm 1) = 0 \tag{21}$$

and the transition conditions at $\Gamma = \bar{\Gamma}$ are

$$\phi^- = \phi^+ \tag{22}$$

$$(\phi')^- = (\phi')^+ \tag{23}$$

$$\eta^- = \eta^+ \tag{24}$$

$$(\phi'')^- = (\phi'')^+ \tag{25}$$

$$(\phi''')^- - (\phi''')^+ = p\lambda^4 \tag{26}$$

The mathematical solution for $\phi(\Gamma)$ depends on one parameter λ in addition to the dimensionless load p. For a homogeneous and isotropic panel, this parameter reduces to

$$\lambda^4 = 48(H/h)^2 \tag{27}$$

where H is the maximum rise of the middle surface. Thus, for the isotropic case, λ is strictly a geometric parameter. A larger value of λ implies a deeper panel. In the laminated orthotropic case, the value of λ depends on the stacking sequence and material properties as well as the rise of the panel.

Solutions

For a specific value of the parameter λ, a closed-form solution for this nonlinear boundary-value problem is obtained. Equation (18) is nonlinear since the dimensionless force resultant η, although spatially constant, depends quadratically on ϕ. In spite of this, the functional form of $\phi(\Gamma)$ may be obtained by techniques used for the solution of linear ordinary differential equations if η is regarded as a constant. In this manner, Eq. (18) is solved in the intervals $-1 < \Gamma < \bar{\Gamma}$ and $\bar{\Gamma} < \Gamma < 1$ subject to conditions (20-26). The jump condition [Eq. (26)] introduces the load parameter p into the solution for $\phi(\Gamma)$. This solution for $\phi(\Gamma)$ is then substituted into Eq. (19) to get a nonlinear relation between η and p. In this process, it is convenient to define a parameter q, called the thrust parameter, and a new load parameter, ξ. These are defined as

$$q^2 = -\eta\lambda^4 \tag{28}$$

$$\xi = p\lambda^4 \tag{29}$$

Real values of q imply negative values of η, which in turn implies that the circumferential arc length is shortened. In the following, solutions are presented for middle surface compression only; i.e., q^2 is restricted to nonnegative values. With this definition of q, the governing equations [(18) and (19)] become

$$\phi'''' + q^2\phi'' = -q^2 \tag{30}$$

$$q^2 = (\lambda^4/2)\int_{-1}^{+1} [\phi - \tfrac{1}{2}(\phi')^2]\,d\Gamma \tag{31}$$

The solution for $\phi(\Gamma)$ from Eq. (30), subject to boundary conditions (20) and (21) and the transition conditions (22-26), takes on various functional forms depending on the value of q. For midspan loading, $\bar{\Gamma} = 0$, these solutions are as follows: For $q = 0$,

$$\phi(\Gamma) = \xi[\,|\Gamma^3|/12 - \Gamma^2/4 + 1/6] \tag{32}$$

For $q = q_n = n\pi/2$, where n is an odd integer,

$$\phi(\Gamma) = A_n^* \cos(q_n\Gamma) - \sin(q_n)(1 - |\Gamma|)/q_n + [1 - \sin(q_n)\sin(q_n|\Gamma|)]/q_n^2 + (1-\Gamma^2)/2 \tag{33}$$

For $q = q_n$, where n is an even integer,

$$\phi(\Gamma) = b\sin(q_n\Gamma) + (1 - \cos(q_n\Gamma)/\cos q_n)/q_n^2 + (1-\Gamma^2)/2 - \xi[1 - |\Gamma| - \sin(q_n|\Gamma|)/q_n]/(2q_n^2) \tag{34}$$

Table 1 Test cases presented

Specimen no.	Layup	Load offset, %	Arc length, in.	λ	Measured Data: Radius, in.	Thickness, in.	A_{22}, lb/in. $\times 10^5$	D_{22}, lb-in.
5	$[(90/0)_3]_s$	0	12	5.68	55.42	0.060	5.85	263.5
6	$[(90/0)_3]_s$	15	12	5.53	55.34	0.062	5.85	265.4

For q positive and not equal to zero or integer multiples of $\pi/2$,

$$\phi(\Gamma) = [1 - \cos(q\Gamma)/\cos q]/q^2 + (1 - \Gamma^2)/2$$

$$- \xi[1 - |\Gamma| - \tan(q)\cos(q\Gamma)/q + \sin(q\Gamma)/q]/(2q^2) \quad (35)$$

These solutions are symmetric in Γ except for Eq. (34), which has an antisymmetric portion multiplied by the coefficient b, the "asymmetric amplitude." Equations (32-35) are substituted into Eq. (31) to get the following results: For $q = 0$, either

$$\xi = 0 \text{ or } 25/4 \quad (36)$$

For $q = q_n$, n odd,

$$A(A_n^*)^2 + B(A_n^*) + C = 0 \quad (37)$$

in which

$$A = 1/(4q_n^2), \quad B = -1/q_n$$

$$C = q_n^2/\lambda^4 - 1/6 + 3/(4q_n^2) - 1/q_n^3 \quad (38)$$

For $q = q_n$, n even,

$$A\xi^2 + B\xi + C = Db^2 \quad (39)$$

in which

$$A = -3/(16q_n^2), \quad B = [1 - \cos q_n]/(2q_n^4)$$

$$C = 1/6 - q_n^2/\lambda^4 - 1/(4q_n^2), \quad D = q_n^2/4 \quad (40)$$

For q positive and not equal to an integer multiple of $\pi/2$,

$$A\xi^2 + B\xi + C = 0 \quad (41)$$

in which

$$A = 3/(16q^2) + \tan^2(q)/(16q^4) - 3\tan(q)/(16q^5)$$

$$B = (1 - \cos q)/(2q^4\cos q) - \tan(q)/(4q^3\cos q)$$

$$C = q^2/\lambda^4 - 1/6 + (4q^2\cos^2 q)^{-1} - \sin(2q)/(8q^3\cos^2 q) \quad (42)$$

Equation (37) determines the coefficients A_n^*, Eq. (39) determines the relation between the asymmetric amplitudes and the load, and Eq. (41) determines the relationship between the load and thrust. It is a simpler procedure to specify q in Eq. (41) and solve for the load ξ.

For the midspan load position, the qualitative character of the load deflection equilibrium paths depend on λ. For $0 < \lambda < 1.976$, the deflection increases monotonically with the load and no instability occurs. For $1.976 < \lambda < 2.825$, a relative maximum load (limit point) occurs on the equilibrium path, and snap-through instability occurs at this limit point. For $\lambda > 2.825$, a secondary path representing asymmetric equilibrium configurations ($b \neq 0$) intersects the primary equilibrium path on the ascending side. The primary path emanates from the origin in the load deflection plot and represents symmetric equilibrium configurations. The intersection point, or bifurcation point, occurs before the limit point is reached on the primary path, and the panel snaps through at the bifurcation point.

The solutions for eccentric load position, $\bar{\Gamma} \neq 0$, follow a similar pattern as a function of q as do the solutions for the midspan load position presented above. Details are given in Ref. 1. Bifurcation does not occur for the load in an offset position. The load deflection path is a single continuous curve with snap-through occurring at a limit point.

Experimental Setup and Procedure

In order to make a comparison of the analytic and experimental results, the conditions of the experiment had to closely approximate the assumptions in the analysis. This required the test specimens to be supported such that their ends remained free of rotational constraints while the distance between the supports remained constant. Also, the load needed to be applied so that it acted radially at the panel middle surface. To meet these requirements, as well as others, specimens, a test fixture, and a test procedure were designed to facilitate a fair comparison between the assumptions of the analysis and the physical realities of the experiment.

Cylindrical Specimens

The test specimens were fabricated using AS4/3502 graphite-epoxy prepreg. (This material is available from Hercules Inc.) Table 1 shows the geometry, stacking sequence, material properties, and testing conditions for the specimens reported on herein. (Tests on other specimens are reported in Ref. 1.) For each geometry to be tested, a large 18 × 24 in. curved panel was fabricated using curved forms. These forms had a radius of curvature, in the 24 in. direction, of 60 in. After curing, each large panel was ultrasonically C-scanned to determine if any irregularities (e.g., voids) were present within the panel. A uniformity of transmittance suggested a uniformity of material in the panel and so the specimens to be tested were machined from these larger panels. Each specimen then had a set of three holes drilled at the point of load application. This will be discussed shortly. By keeping a close tolerance on the arcwise location of the holes, it was possible to control the amount of load eccentricity. Slotted dowels, 0.374 in. in diameter (to be discussed further in connection with the test fixture), were then attached to each end of the specimen. Finally, strain gages were mounted on the specimens. Several back-to-back gage pairs at various arc-length locations were used to monitor bending and in-plane strains.

Test Fixture

Figure 2 shows side- and end-view schematics of the test fixture, while Fig. 3 shows a photograph of the fixture. The major components of the fixture are: end dowels, support blocks, base plate, loading head and pivot, and tongue and connector.

End Dowels

The end dowels were 0.375-in.-diam steel rods slotted to accommodate the ends of the curved panels. The dowels were one part of a system designed to accurately represent a simple support condition. The ends of the panel were potted solidly in the dowel slots using epoxy. The epoxy prevented the ends of the panel from brooming under the in-plane compressive thrust loads. The rods were slotted along a rod radius and the panels were centered, using shims if necessary, within the slots. With care, the end of the middle surface of the panel could be made to coincide with the centerline of the dowel.

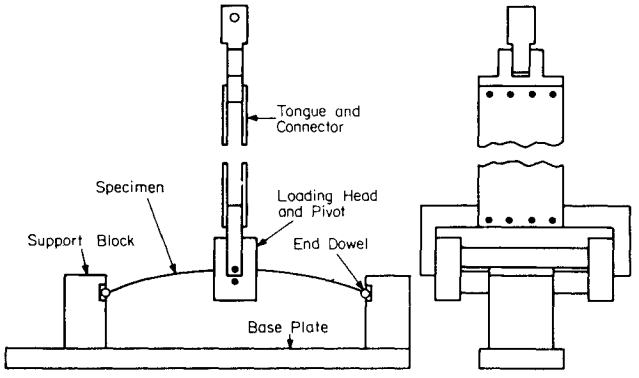

Fig. 2 Schematic of test fixture.

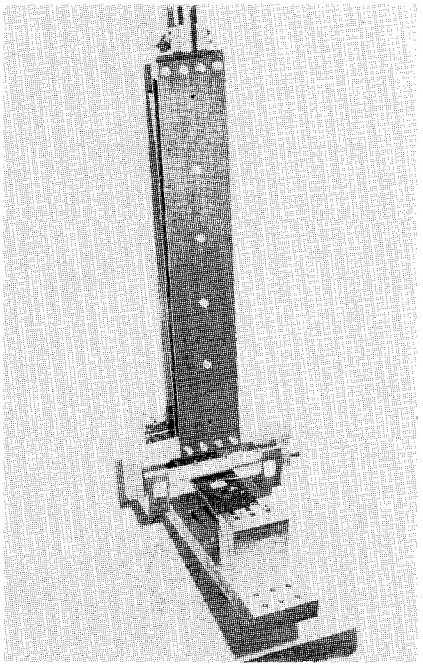

Fig. 3 Photograph of test fixture.

With this arrangement, the boundary conditions at the ends of the middle surface ($\theta = \pm\beta$) could be accurately enforced.

Support Blocks

The support blocks provided the moment-free support conditions on the ends of the specimen and they provided restraints so that the horizontal distance between the supports remained fixed. The in-plane thrust loads generated as the panels deformed tended to force the ends of the panel into the support blocks. This end force, coupled with friction, could induce an unwanted moment at the end of the panel. Also, the thrust loads could spread the support blocks apart and thereby violate the constant distance assumption. Thus the support mechanism had to be stiff and yet allow for frictionless support of the panel. The design adapted consisted of roller bearings mounted in steel blocks. There were six roller bearings in each block and the bearings were situated so the dowels on the ends of the specimens were forced against them. There were actually three bearings in a line above the end dowel and three bearings in a line below it. Figure 4 shows a photograph of one support block. This arrangement worked satisfactorily.

Base Plate

The base plate formed the backbone of the fixture, providing stiffness for the fixture and a solid foundation for locating the support blocks. The primary consideration in designing the entire fixture was to accommodate small deviations in specimen geometry, i.e., deviations from intended geometry. It is difficult to fabricate and cut curved panels exactly as intended and this was recognized. Thus, the base plate was designed to allow for variations in the 6- and 12-in. arc lengths of the panels. One of the two support blocks was fixed to the base plate with hardened steel pins and bolts. The steel pins passed through the base plate and into the support block, preventing slippage of the support block relative to the base plate. The bolts held the block down onto the plate. The other block was bolted to the base via slotted holes in the base. The slots permitted spanwise adjustments in the support-block position to accommodate the deviations in panel geometry.

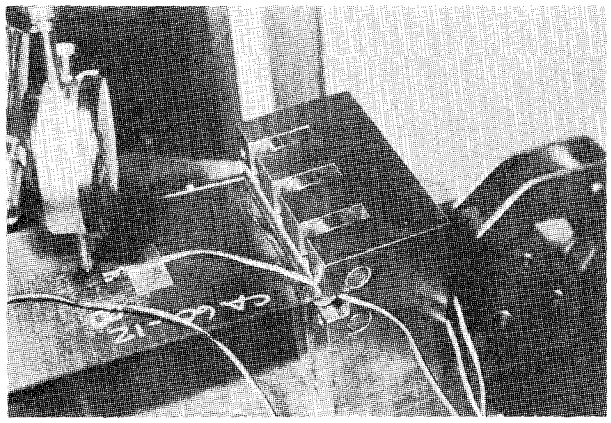

Fig. 4 Photograph of support block.

Loading Head and Pivot

The analysis assumed that the panel was subjected to a line load applied at the geometric middle surface. There were two difficulties achieving this ideal. First, it was physically impossible to contact the geometric middle surface. A line load acting radially from above would contact the outer surface of the panel. This would result in a slight offset between the location the load was assumed to act and where it actually did. This is not serious until the cross section of the panel at the line load location begins to rotate. Then this effect, coupled with the load, would induce a small moment in the panel, in addition to the line load. This could have been accounted for in the analysis but such a moment was deformation-dependent, making the governing equations more difficult to solve. Thus, to have the line load act at the geometric middle surface, a novel loading mechanism was adapted. Incorporated into this mechanism was a scheme to ensure against the second problem, namely, that no moment be transferred into the panel through the loading fixture. The loading head and pivot fork used to transmit a pure line load to the geometric middle surface of the panel are shown schematically in Fig. 2 and in the photograph of Fig. 3. Three small bolts through the panel and the large dowels secured the arcwise location of the line road. Centering the panel in the gap between the large dowels guaranteed that the line of pivoting passed through the geometric middle surface. Of course the pivots themselves prevented any moment from being transferred to the panel.

Tongue and Connector

The pivot fork was attached to the bottom end of two long steel plates. The long plate assembly, or tongue, is shown in Figs. 2 and 3. In the analysis it was assumed that the line load moved downward radially and deflected the panel, with the simply supported ends of the panel remaining stationary. In the experiment, the vertical displacement of the panel at the location of the line load was held to zero and the simply supported ends moved upward. Due to the assumed shallowness of the panels tested, this was essentially the same as holding the radial displacement to zero at this point. The tongue was

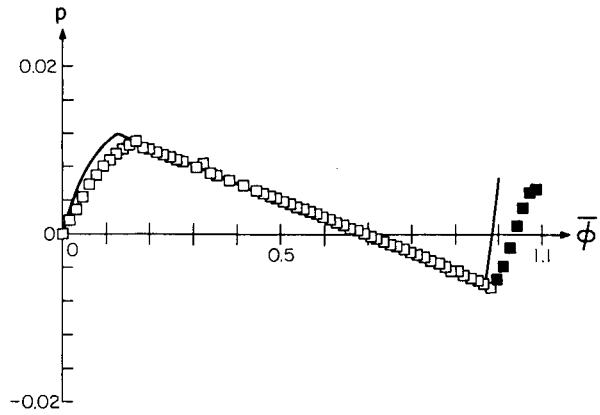

Fig. 5 Comparison of theory and experiment: load displacement for $\bar{\Gamma}=0$ and $\lambda=5.68$.

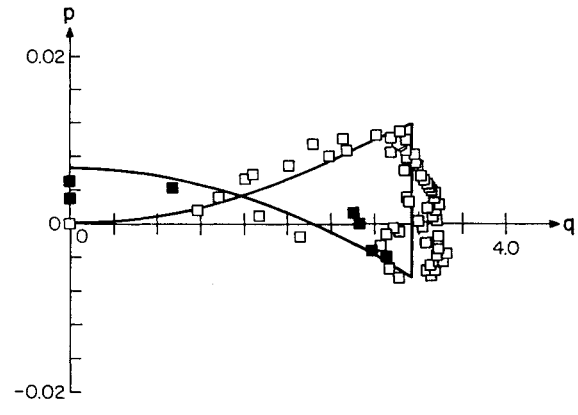

Fig. 6 Comparison of theory and experiment: load thrust for $\bar{\Gamma}=0$ and $\lambda=5.68$.

used to attach the panel to the stationary upper head of the load frame. The base plate rested on the lower movable head. To deform the panel, the lower head was moved upward. The tongue was made as long as possible for the following reason: As the panel deformed, tangential (u) displacements resulted. This meant that the line load position moved tangentially. In the analysis it was assumed that the line load acted strictly in a radial direction. To do this the line load must translate tangentially, the line of action remaining parallel to the original no-load direction. Experimentally it was very difficult to translate the line load tangentially. An infinitely long tongue, fixed at the top and attached to the panel at the bottom, would satisfy this requirement. Practically speaking, a long tongue is all that was possible. The maximum tongue length was dictated by the physical dimensions of the load frame. A connector simply attached the upper end of the tongue to a universal joint and, ultimately, the fixed upper head. In Fig. 3 the connector attached to the tongue is visible at the top of the photograph.

In reality, the issue of radial acting load vs nonradial acting load was not a problem. Due to the assumption in the analysis that the cylindrical panels were of shallow curvature, any load that acted within the semiopening angle of the purely radial direction produced the same theoretical response as a pure radial load. Thus, with the tongue setup, the load would be assumed to act radially to within the accuracy of the theory.

Initial Measurements and Experimental Procedure

Before the actual testing of a specimen began, some initial measurements related to geometry and material properties were taken. Arc length, width, and thickness of each specimen were measured. Also, the location of the centers of the three holes for attaching the loading head was measured. Tensile and bending tests were conducted to determine the elastic properties of each specimen. The bending stiffness, D_{22}, to be used in the theory was determined by three-point bend tests on the actual specimen. A tensile test of a 0.5 × 12 in. strip cut from the 18 × 24 in. curved panel was used to determine the in-plane property, A_{22}. This strip was cut from the cylindrical panel in the generator direction and the quantity A_{11} was measured. For the stacking sequences used here, A_{11} and A_{22} should have been equal. To measure A_{22} directly would have required a complex testing rig. Thus the value of A_{22} was assumed to be the measured value of A_{11}. The values of A_{22} and D_{22} for the specimens reported here are shown in Table 1.

After the specimen was mounted in the test fixture, its radius of curvature was measured. Even though each specimen was to have a 60 in. radius, temperature differences through the thickness of the curing laminate, slight variations in volume fractions, slight fiber misalignments, and other factors all would contribute to produce a radius slightly different than 60 in. Also, when mounting the curved specimens in the fixture, a slight movement of the support blocks toward each other could dramatically change the curvature of the mounted specimen. The radius of curvature of the mounted specimen was measured with a dial gage and a traverse mechanism that moved the dial gage along the span of the curved panel. A least-squares radius of curvature was determined from the data.

After the radius of curvature was measured, the strain gages were balanced and nulled. The loading head was then attached. This process would undoubtedly induce small strains in the panels. The strain gages were then nulled by moving the loading head up or down with the load frame controls to eliminate the slight initial deflection caused by attaching the load. This condition was the data, the load, strains, and displacements being zero.

Correlation of Experimental and Theoretical Results

To make the comparison with the experiment clearer, the analytic results shown represent only those configurations assumed to be stable. The initial measurements made on the test specimens concerning the geometry and material properties were used in generating the analytical curves presented with experimental results. Also, the small initial strain in the panels, due to fitting the specimens into the fixture, has been subtracted from the experimental data presented. In all tests performed this initial strain was less than 50 $\mu\epsilon$ in magnitude, or less than 2.5% of the maximum strain. Both experimental and analytical results are presented in nondimensional form.

Comparison of the analytical and experimental results for the two $[(90/0)_3]_s$ specimens shown in Table 1 are presented here. For specimen 5 the load is positioned at midspan, and for specimen 6 the load is positioned at a 15% offset ($\bar{\Gamma}=0.15$). Otherwise, the data in Table 1 show these two specimens to be almost the same.

It should be mentioned that there were problems during testing of the four-ply $[90/0]_s$ laminates. It appeared that friction generated at the supports for these thin laminates was sufficient to constrain the rotation of the ends.

Midspan Loading

Figure 5 shows the load-displacement response for specimen 5. The dimensionless radial displacement at the point of load application, $\bar{\phi}$, is plotted on the abscissa. To aid in interpreting the magnitude of the displacements, values of $\bar{\phi}$ near unity imply a physical displacement of order $2H$, where H is the maximum rise. The analytic predictions are shown as solid lines and the experimental data are shown by opened and darkened symbols. The darkened symbols correspond to equilibrium configurations in which the thrust is decreasing from a maximum as the displacement increases.

The theory predicts bifurcation behavior for the value of λ shown in Fig. 5. The straight line with negative slope is the

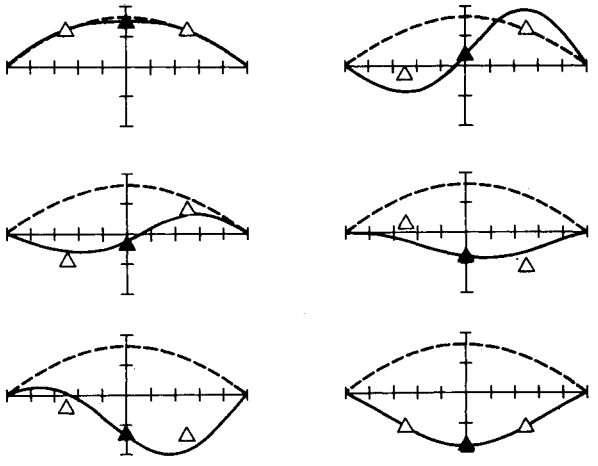

Fig. 7 Comparison of theory and experiment: equilibrium configurations for $\bar{\Gamma}=0$ and $\lambda=5.68$.

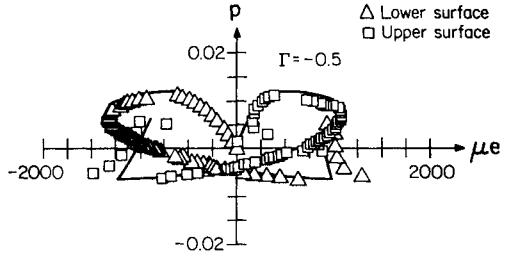

Fig. 8 Comparison of theory and experiment: load vs surface strains at $\Gamma=-0.5$ for $\bar{\Gamma}=0$ and $\lambda=5.68$.

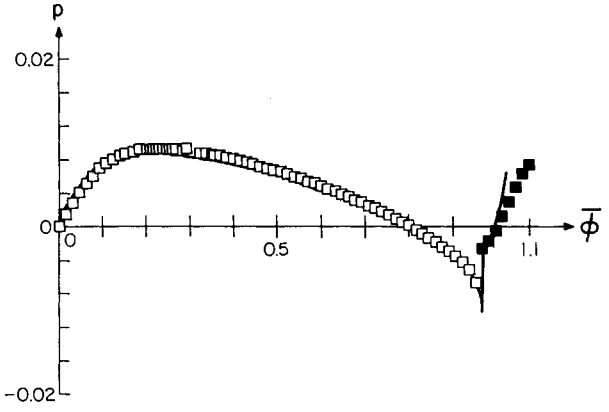

Fig. 9 Comparison of theory and experiment: load displacement for $\bar{\Gamma}=0.15$ and $\lambda=5.53$.

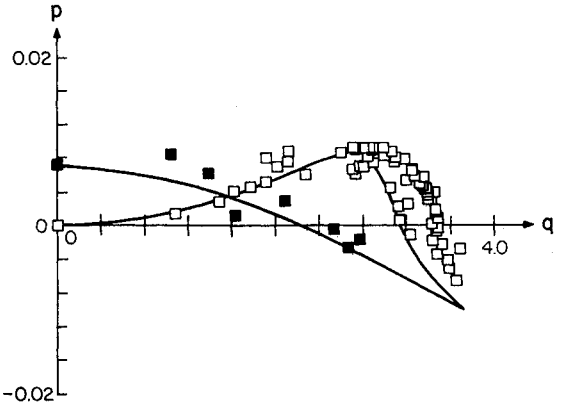

Fig. 10 Comparison of theory and experiment: load thrust $\bar{\Gamma}=0.15$ and $\lambda=5.53$.

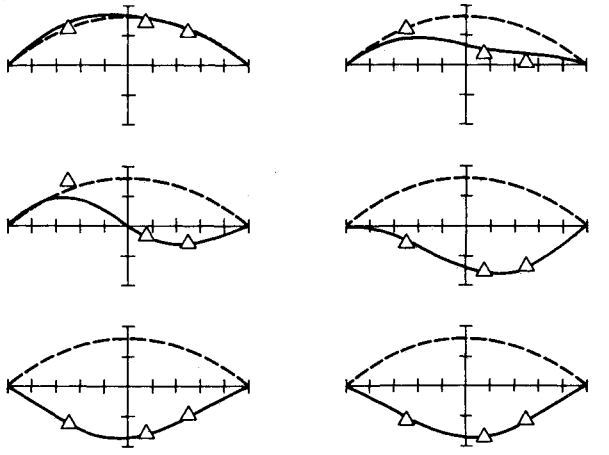

Fig. 11 Comparison of theory and experiment: equilibrium configurations for $\bar{\Gamma}=0.15$ and $\lambda=5.53$.

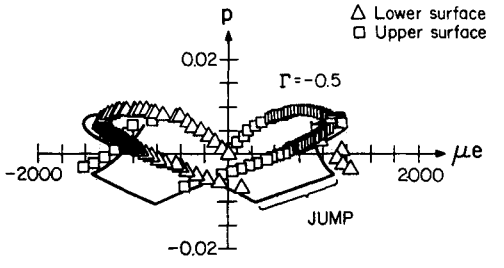

Fig. 12 Comparison of theory and experiment: load vs surface strains at $\Gamma=-0.5$ for $\bar{\Gamma}=0.15$ and $\lambda=5.53$.

secondary equilibrium path corresponding to asymmetric equilibrium configurations. [Refer to Eqs. (34) and (39).] This secondary path intersects the primary equilibrium path at the two bifurcation points. The primary path corresponds to symmetric configurations. [Refer to Eqs. (32), (33), (35-37), and (41).] The experimental data do not exhibit bifurcation behavior, but show one continuous equilibrium path with two limit points. Since bifurcation behavior is a mathematical result of an analysis of the perfect structure subject to perfectly symmetric loading, it is not observed in even carefully conducted experiments because of small imperfections. Here the load position was carefully controlled. However, due to manufacturing tolerances and the procedure required to fit the panel in the test fixture, the deviation of the initial shape from a perfect circle was much less controllable. Figure 5 shows that the correlation between theory and experiment is quite good, which implies that the imperfection of the specimen was small.

Figure 6 shows the load-thrust results for specimen 5. In the analysis the thrust is spatially constant. Experimentally this was not quite true, and at a given load the average value for q was computed from all back-to-back strain-gage locations and is plotted in Fig. 6. In addition, the theory shows that the thrust is constant along the secondary path [$q=\pi$ and $b\neq 0$ in Eqs. (34) and (39)]. This accounts for the vertical line at $q=\pi$ in Fig. 6. since the experiment cannot duplicate this idealized bifurcation behavior, deviation between theory and experiment is expected.

Figure 7 shows the deformed shapes of the middle surface (solid lines) with respect to the undeformed configuration (dashed lines) as the load increases. The open symbols in these figures represent test data obtained from dial gages. The asymmetric configurations predicted from theory correspond to the secondary equilibrium path. The greatest discrepancy between theory and experiment is when the theory predicts configurations from the secondary path.

Figure 8 shows the upper and lower surface strains as a function of the load at the quarter-point $\Gamma=-0.5$. The agreement between theory and experiment is very good.

Eccentric Loading

Figures 9-12 show the results for the $[(90/0)_3]_s$ laminate with 15% load offset. The correlation between theory and experiment is excellent. There is only one continuous equilibrium path predicted from the theory. This path is not entirely stable in displacement-controlled loading, however. A vertical tangent occurs on the load-displacement plot near $\bar{\phi} = 0.95$ in Fig. 9. A small increase in the displacement at this vertical tangency point causes a jump to a different portion of the same path which has larger values of $\bar{\phi}$. Evidence of this behavior can also be seen by carefully examining the spatial configurations shown in Fig. 11.

Concluding Remarks

The experiment verified that the analysis of a shallow elastic arch made from homogeneous and isotropic materials is applicable to the shallow orthotropic panel. (The elastic constants in the constitutive equations have to be changed from a beam theory to a shell theory, however.) The single parameter λ governs the behavior of the solution. For an isotropic and homogeneous material, λ is a function of panel geometry only. For orthotropic bidirectional laminats, λ depends on the material properties and stacking sequence as well as the geometry. The panel response may exhibit no instability, snap-through instability at a limit point, or snap-through instability at a bifurcation point, depending upon the value of λ.

A test fixture was carefully designed to duplicate the conditions in the analysis. However, the loading device was designed to control the displacement at the line of application of the load rather than the magnitude of the force. A greater portion of the equilibrium path is stable for displacement control than for force control. Consequently, the limit point loads were more precisely determined in the experiment using this loading apparatus. Very good correlation between theory and experiment was achieved using this test fixture for most of the laminates in this study. It proved impossible, though, to obtain accurate results for the thin, four-ply laminates with this experimental setup. This was due to the friction generated at the supports, even though significant effort was devoted to minimize friction.

Initial geometric imperfections in the shape of the panels caused the response for midspan loading to be slightly asymmetric. Consequently, a limit point, or maximum load, occurred on the equilibrium path rather than a bifurcation point predicted from the theory. The load at the limit point is less than the load at the bifurcation point. This reduction is important and is consistent with the theoretical results of Shreyer.[6] Also, reduced snap-through loads are obtained for slightly offset load positions from midspan; this is consistent with the work of Plaut.[7]

Acknowledgments

The research effort leading to the results presented herein was financially supported by the NASA Langley Research Center's Impact Dynamics Branch through the NASA-Virginia Tech Composites Program, Cooperative Agreement NCC1-15. This support is gratefully acknowledged. The technical assistance of Robert G. Thompson, Huey D. Carden, and Richard L. Boitnott of the Impact Dynamics Branch is appreciated. Also the machine-shop support of Robert L. Davis at Virginia Tech is appreciated.

References

[1]Carper, D. M., Hyer, M. W., and Johnson, E. R., "Large Deformation Behavior of Long Shallow Cylindrical Composite Panels," Virginia Polytechnic Institute and State University, Blacksburg, VA, VPI-E-83-37, Sept. 1983.

[2]Biezeno, C. B. and Grammel, R., *Engineering Dynamics*, Vol. 2, Blackie and Sons, London, 1956, p. 397.

[3]Fung, Y. C. and Kaplan, A., "Buckling of Low Arches or Curved Beams of Small Curvature," NACA TN-2840, 1952.

[4]Schreyer, H. L., and Masur, E. F., "Buckling of Shallow Arches," *Journal of the Engineering Mechanics Division*, Vol. 92, No. EM4, Aug. 1966, pp. 1-19.

[5]Cheung, M. C. and Babcock, C. D. Jr., "An Energy Approach to the Dynamic Stability of Arches," *Journal of Applied Mechanics*, Vol. 37, Dec. 1970, p. 1012.

[6]Schreyer, H. L., "The Effect of Initial Imperfections on the Buckling Load of Shallow Circular Arches," *Journal of Applied Mechanics*, Vol. 39, June, 1972, p. 445.

[7]Plaut, R. H., "Influence of Load Position on the Stability of Shallow Arches," *Journal of Applied Mathematics and Physics (ZAMP)*, Vol. 30, 1979, p. 548.

[8]Nash, W. A. and Hus, M.Y.H., "Stresses and Deflections in a Composite Material Arch," *Proceedings of the 5th International Conference on Experimental Stress Analysis*, edited by Prof. G. Bartolozzi, Udine, Italy, May 1974, p. 2.63.

[9]Marshall, I. H., Rhodes, J., and Banks, W. M., "Experimental Snap-Buckling Behavior of Thin GRP Curved Panels Under Lateral Loading," *Composites*, Vol. 8, No. 2, April 1977, p. 81.

[10]Simitses, G. J., *An Introduction to the Elastic Stability of Structures*, Prentice-Hall, Englewood Cliffs, NJ, 1976, pp. 189-196.